ACS APPLIED MATERIALS & INTERFACES

Research Article

www.acsami.org

Low-Surface-Area Hard Carbon Anode for Na-Ion Batteries via Graphene Oxide as a Dehydration Agent

Wei Luo,[†] Clement Bommier,[†] Zelang Jian,[†] Xin Li,[†] Rich Carter,[†] Sean Vail,[‡] Yuhao Lu,[‡] Jong-Jan Lee,[‡] and Xiulei Ji*,[†]

[†]Department of Chemistry, Oregon State University, Corvallis, Oregon 97331, United States

[‡]Sharp Laboratories, Inc., Camas, Washington 98607, United States

Supporting Information

ABSTRACT: Na-ion batteries are emerging as one of the most promising energy storage technologies, particularly for grid-level applications. Among anode candidate materials, hard carbon is very attractive due to its high capacity and low cost. However, hard carbon anodes often suffer a low first-cycle Coulombic efficiency and fast capacity fading. In this study, we discover that doping graphene oxide into sucrose, the precursor for hard carbon, can effectively reduce the specific surface area of hard carbon to as low as 5.4 m^2/g. We further reveal that such doping can effectively prevent foaming during caramelization of sucrose and extend the pyrolysis burnoff of sucrose caramel over a wider temperature range. The obtained low-surface-area hard carbon greatly improves the first-cycle Coulombic efficiency from 74% to 83% and delivers a very stable cyclic life with 95% of capacity retention after 200 cycles.

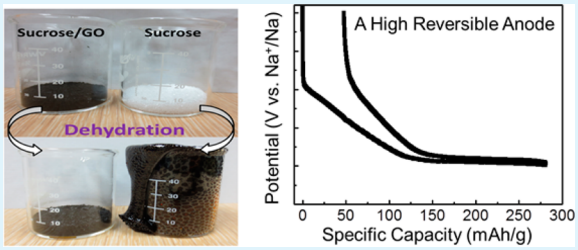

KEYWORDS: *hard carbon, Na-ion batteries, anode, low surface area, high first-cycle Coulombic efficiency*

INTRODUCTION

Advanced energy storage devices are the key enabler for renewable energy sources, including wind and solar power, as well as for the realization of electric transportation. Ideally, they should exhibit high energy/power density and are of low cost and great safety properties. Among different devices, Li-ion batteries (LIBs) have been intensively pursued as power sources for portable electronic devices and electric vehicles (EVs) due to their high energy/power density and long cycle life.[1−3] However, the rarity and being geographically concentrated of lithium resources may severely restrict LIBs' perspective applications in grid-level energy storage.[4] Currently, attention is starting to shift to Na-ion batteries (NIBs),[5−7] which exhibit slightly inferior performance metrics compared to LIBs due to the lower cell voltages and less capacities. However, NIBs represent a great fit for grid-level storage because they are potentially very cost-effective due to the abundance and wide distribution of sodium resources. Furthermore, NIBs can utilize inexpensive aluminum current collectors for anodes whereas LIBs have to use copper.[8−10]

Over the past few years, significant progress has been made for NIB cathodes by updating the knowledge learned from LIB studies.[11−15] However, with respect to anodes, graphitic carbon, the commercial LIB anode, does not function well for NIBs due to its extremely low capacity, ∼31 mAh/g, according to the formation of NaC_{70} upon sodiation.[16,17] It is the large ionic size of Na^+, ∼98−102 pm (depending on the coordination number), that causes such a low capacity.[18,19] Alternatives, including metal alloys,[20−24] metal oxides[25−27] or sulfides,[28−30] can provide much higher capacities than carbon-based anodes. However, they often exhibit less favorable high redox potentials and, sometimes, low first-cycle Coulombic efficiency. Among the candidates for NIB anodes, carbon-based materials still hold promise, considering the cost for the potential scaling up, and the most promising one is expected to be hard carbon.

Hard carbon, also known as nongraphitizable carbon, is very difficult to be graphitized, even at a temperature higher than 2000 °C.[31,32] Its structure typically comprises small turbostratic nanodomains with nanosized voids sitting in between these nanodomains.[32] Pioneering studies have demonstrated promising performance of hard carbon as anodes for both LIBs and NIBs with low operating potentials and relatively high specific capacities.[33−36] Unfortunately, hard carbon usually suffers a low first-cycle Coulombic efficiency, lower than 75%, and fast capacity fading over cycling. To date, much attention has focused on fabricating functional carbon nanostructures with high surface areas, which can enhance the rate capability by facilitating better contacts between the electrolyte and the electrode.[37−39] However, the first-cycle Coulombic efficiency is typically very low for these carbon anodes.[40−42] The poor efficiency may be caused by the more prominent formation of solid electrolyte interphase (SEI) layer on the large surface area.[43,44] This can be a serious issue because the low first-cycle Coulombic efficiency of anodes causes the irreversible loss of

Received: November 3, 2014
Accepted: January 6, 2015
Published: January 6, 2015

DOI: 10.1021/am507679x
ACS Appl. Mater. Interfaces 2015, 7, 2626−2631

active Na^+ ions, provided by the cathode, which decreases the full-cell capacity. It is well-known that a lower surface area increases the first-cycle Coulombic efficiency for carbon anodes in LIBs.[45−47] However, an effective strategy to minimize the surface area of hard carbon remains a significant challenge.[48]

Sucrose is a typical precursor for producing hard carbon due to its abundance, low cost and renewability.[48,49] The conventional synthesis of hard carbon from sucrose consists of two steps: dehydration and pyrolysis. During the dehydration, water from sucrose caramelization is eliminated to a large degree at a modest temperature, e.g., 180 °C. The following pyrolysis is normally carried out under an inert gas at temperatures, ranging from 900 to 1600 °C. It has been reported that the specific surface area of hard carbon decreases upon using high pyrolysis temperatures, e.g., 1400 to 1600 °C.[50,51] However, a high-temperature treatment not only raises the cost but sometimes reduces the reversible capacity.[52,53] Therefore, it is critical to find an alternative method that is effective to reduce the surface area of hard carbon at a relatively low pyrolyzed temperature.

Herein, we report an effective strategy to minimize the surface area of sucrose-derived hard carbon simply by introducing graphene oxide (GO) suspension into the sucrose solution. We discover that a hard carbon of surprisingly low specific surface area, e.g., 5.4 m^2/g, can be prepared by pyrolysis of such a mixture of sucrose/GO. In sharp contrast, hard carbon derived from sucrose powder shows a much higher specific surface area of 137.2 m^2/g. When evaluated as an anode for NIBs, sucrose/GO derived hard carbon, referred to as G-HC, exhibits a much enhanced first-cycle Coulombic efficiency of 83% compared to that of sucrose derived hard carbon (designated as HC), 74%. Furthermore, G-HC shows a high desodiation capacity of 280 mAh/g and very stable cycling performance over ∼200 cycles with capacity retention of ∼95%, whereas HC exhibits a fast capacity fading.

EXPERIMENTAL SECTION

Materials Synthesis. For synthesis of G-HC, GO aqueous suspension is first prepared via a modified Hummer's method.[54,55] Then, sucrose is dissolved in the GO aqueous suspension (mass ratio of sucrose/GO is 80:1) under sonication. The resulting sucrose/GO solution is dried at 80 °C, dehydrated at 180 °C for 24 h and then pyrolyzed at 1100 °C for 6 h under Ar. In a control experiment, sucrose powder is directly dehydrated at 180 °C for 24 h and pyrolysis at 1100 °C for 6 h under Ar.

Materials Characterization. X-ray diffraction (XRD) patterns are collected using a Rigaku Ultima IV Diffractometer with Cu Kα irradiation (λ = 1.5406 Å). The morphology is examined by scanning electron microscopy (SEM, FEI, Quanta 600F). N_2 sorption measurements are performed on a TriStar II 3020 analyzer. Thermogravimetric analysis (TGA) is performed under Ar from ambient temperature to 1000 °C (ramp rate: 10 °C/min).

Electrochemical Measurements. The electrodes consist of hard carbon active mass and polyvinylidene fluoride (PVDF) binder with or without carbon black additive. For preparation of the electrodes, hard carbon was ground in a mortar for 10 min, and then a PVDF/NMP solution was added for further 30 min of grinding. The as-obtained hard carbon/PVDF slurry was coated on Al foil by a doctor blade and dried at 120 °C under vacuum for 12 h. The mass loading of hard carbon is about 2.5 mg/cm^2 with a thickness of ∼40 μm. Coin cells, 2032-type, were assembled with sodium pellets as the counter/reference electrodes and 1.0 mol/L $NaPF_6$ solution in ethylene carbon (EC)/diethyl carbonate (DEC) (1:1 in volume) as the electrolyte. Galvanostatic cycling in a potential window of 0.01−2 V versus Na^+/Na is conducted on an Arbin BT2000 system at room temperature.

RESULTS AND DISCUSSION

Both G-HC and HC exhibit a typical amorphous carbon structure, revealed by the XRD patterns with two broad peaks, indexed to the (002) and (101) planes, respectively (Figure 1a). Close observation of the XRD patterns indicates that the

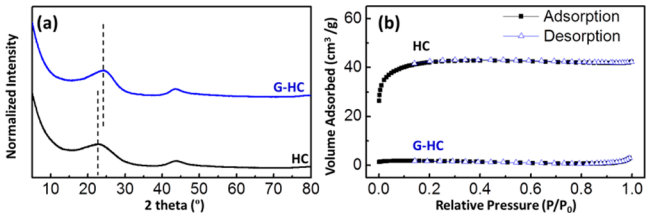

Figure 1. (a, b) XRD patterns and nitrogen adsorption/desorption isotherms of HC and G-HC.

(002) diffraction in HC locates at 2θ of 22.8°, which corresponds to an interlayer spacing of 0.39 nm. Interestingly, the (002) peak of G-HC shifts to 24.0°, suggestive of a smaller interplanar distance of 0.37 nm. N_2 adsorption/desorption measurements are carried out to determine the specific surface area of G-HC and HC. As shown in Figure 1b, HC exhibits a Type I sorption isotherm, suggestive of some microporous porosity with a Brunauer−Emmett−Teller (BET) surface area of 137.2 m^2/g. In sharp contrast, G-HC exhibits a surprisingly low BET surface area of 5.4 m^2/g. The SEM images reveal that both G-HC and HC consist of bulk particles (Figure 2a,c). Moreover, despite the much higher surface area, HC exhibits a much smoother surface, compared to that of G-HC, as the zoomed-in SEM images show (Figure 2b,d).

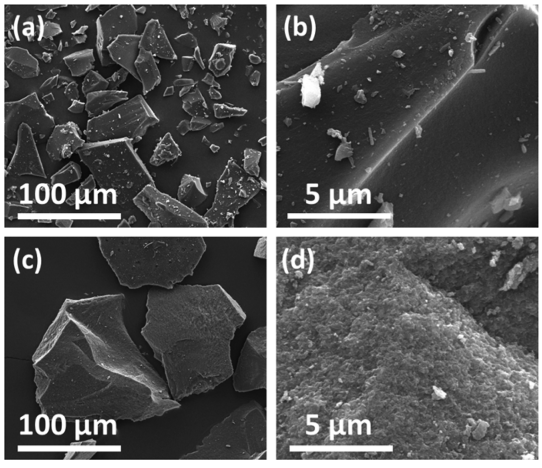

Figure 2. SEM images of HC (a, b) and G-HC (c, d) at different magnifications.

It has been reported that the introduction of graphene normally increases the surface area of the composites due to the high theoretical surface area of single-layer graphene, 2630 m^2/g.[56−58] It is quite interesting that adding GO into sucrose dramatically decreases the specific surface area of the hard carbon product. To investigate this interesting phenomenon, we look back to the synthesis procedure. For preparing hard carbon directly from sucrose powder, the dehydration step is critical because it can improve the yield and simplify the sample handling process. The dehydration step is very similar to the caramelization process, where volume expansion of table sugar

DOI: 10.1021/am507679x
ACS Appl. Mater. Interfaces 2015, 7, 2626−2631

occurs during melting and foaming. As expected, sucrose is turned into foamed caramel after dehydration (Figure 3a).

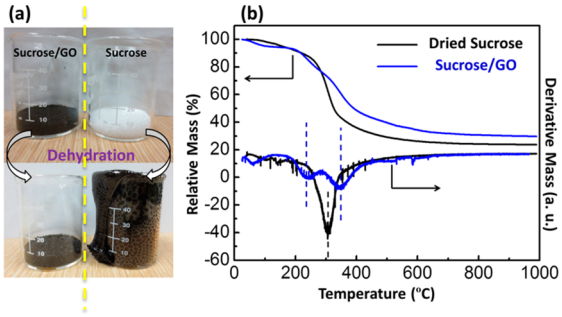

Figure 3. (a) Digital picture of the dried fine mixture of sucrose/GO from its solution (left) and sucrose powder (right) before and after dehydration at 180 °C for 24 h. (b) TGA and differential TGA results comparing the pyrolysis behavior of sucrose/GO mixture and dried sucrose from its solution at a ramp rate of 10 °C/min under Ar.

However, such a foaming phenomenon is not observed when dehydrating the mixture of sucrose/GO (Figure 3a). The mixture of sucrose/GO is obtained by drying its aqueous suspension/solution at 80 °C, which begs a question whether such a solution-to-solid drying process is why foaming does not take place. In a control experiment, a sucrose aqueous solution is also dried at 80 °C, which results in viscous syrup rather than a solid in contrast to the case of sucrose/GO mixture. When the drying temperature is increased to 110 °C, a solid forms out of viscous syrup but foams dramatically (Figure S1, Supporting Information). The dried sucrose obtained from its aqueous solution at 110 °C is further dehydrated and pyrolyzed, yielding a carbon, referred to as HC-S that exhibits a very high specific surface area of 510.2 m^2/g (Figure S2, Supporting Information).

From the observations above, it is evident that GO plays a major role in preventing the foaming process during drying and dehydration. To further investigate this phenomenon, we compared different mass ratios between sucrose and GO during mixing (Table 1). When the mass ratio of sucrose/GO is N, the suspension/solution is referred to as SG-N. Drying SG-1000 at 80 °C results in a viscous syrup, similar to what happens when drying a pure sucrose solution. At 110 °C, SG-1000 foams as well and its final carbon product exhibits a specific surface area of 257.6 m^2/g. Interestingly, SG-200 can be dried into a firm solid at 80 °C without foaming, and as expected, its carbon product exhibits a specific surface area as low as 4.8 m^2/g, even lower than that of G-HC (the product of SG-80), 5.4 m^2/g. SG-10 can be dried at 80 °C without foaming as well. The specific surface area of this carbon sample bounces back to 37.2 m^2/g. However, it is still much lower than that of the hard carbon obtained without GO addition.

To gain further understanding on why the sucrose/GO mixture gives a low surface area, TGA is carried out under Ar for dried sucrose with and without GO. As shown in Figure 3b, the derivative of the TGA results reveal two peaks at ~230 and 350 °C for the dried sucrose/GO mixture whereas the dried sucrose only exhibits one sharp peak at ~305 °C. It appears that GO helps spread the burnoff of sucrose during pyrolysis over a much wider temperature range. In summary, without foaming during dehydration, a burnoff over a wider temperature range facilitates the much lower specific surface area of G-HC. We hypothesize that volatile molecules, including water, generated during dehydration and pyrolysis migrate out along GO nanosheets without creating pores. Further research is ongoing in our lab to investigate this phenomenon.

We evaluate the Na-ion storage properties of the as-obtained hard carbons. Working electrodes are only composed of G-HC or HC (93 wt %) active mass and PVDF binder (7 wt %), which is to avoid the impact from carbon black additive on the first-cycle Coulombic efficiency. Galvanostatic desodiation/desodiation cycling is first performed at a current density of 20 mA/g in a potential window of 0.01−2 V versus Na^+/Na. As previously reported for typical hard carbon anodes in NIBs, HC exhibits two distinct potential regions in the first sodiation profile (Figure 4a). As proposed by Dahn et al., the sloping

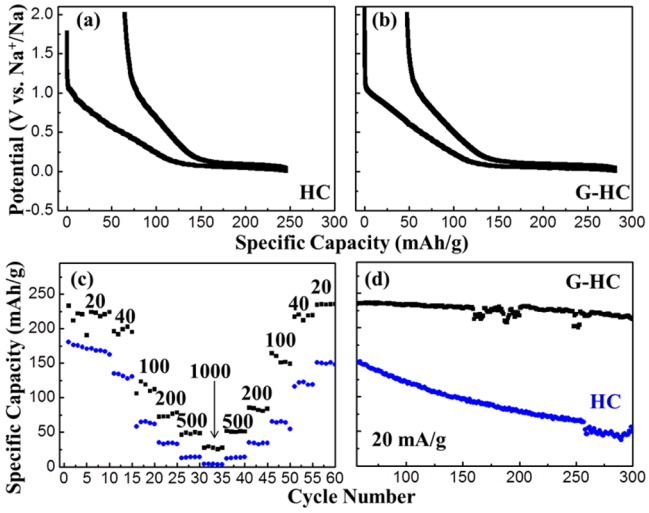

Figure 4. Galvanostatic sodiation/desodiation profiles of the first cycles of HC (a) and G-HC (b) tested in the potential range of 0.01−2 V at a current density of 20 mA/g. (c) Rate and (d) cycling performance of HC (blue) and G-HC (black) tested at current densities from 20 to 1000 mA/g and then at 20 mA/g for long-term cycling in the potential range of 0.01−2 V.

Table 1. Experimental Conditions and BET Surface Areas of the Hard Carbons Derived from Sucrose Powder, Pure Sucrose Solution and Sucrose/GO Suspension/Solution

sample no.	precursor	mass ratio of sucrose/GO	drying temperature of the solution (°C)	BET surface area of the carbon product (m^2/g)
HC	sucrose powder	no GO	N/A	137.2
HC-S	pure sucrose solution	no GO	110	510.2
SG-10	sucrose/GO solution	10	80	37.2
SG-80 (G-HC)	sucrose/GO solution	80	80	5.4
SG-200	sucrose/GO solution	200	80	4.8
SG-1000	sucrose/GO solution	1000	110	257.6

DOI: 10.1021/am507679x
ACS Appl. Mater. Interfaces 2015, 7, 2626−2631

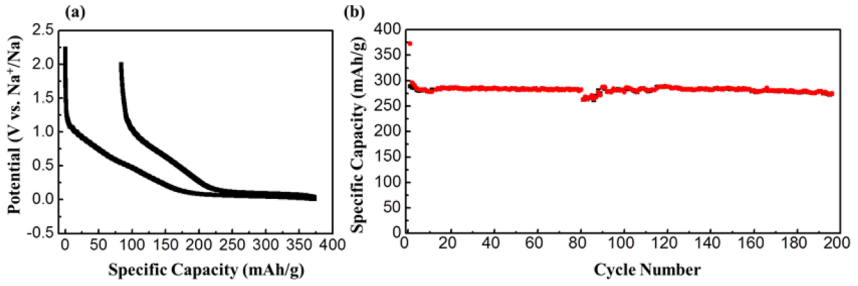

Figure 5. Electrochemical performance of G-HC electrodes with 10 wt % carbon black addition: (a) galvanostatic sodiation/desodiation profiles of the first cycles at 20 mA/g; (b) long-term cycling performance at 20 mA/g in the potential range of 0.01−2 V.

region from 2.0 to ∼0.15 V corresponds to the insertion of Na^+ ions into the interlayers inside the small turbostratic nanodomains along with the SEI formation, whereas the plateau region near 0.1 V is attributed to the process when Na^+ ions "adsorbs" into the nanovoids in between the turbostratic nanodomains.[35] The overall first sodiation capacity is 245 mAh/g, where the contributions from the sloping and plateau regions are 130 and 115 mAh/g, respectively. The following desodiation delivers a capacity of 181 mAh/g, yielding a first-cycle Coulombic efficiency of 74%. Moreover, the capacity contribution from the sloping region in the sodiation profile (from ∼0.15 to 2.0 V) is 87 mAh/g. Subtracting 87 mAh/g from 130 mAh/g, the capacity from the sloping region during first sodiation, there is an irreversible capacity loss of 43 mAh/g. As shown in Figure 4b, G-HC also exhibits similar characteristic potential profiles of hard carbon. The first sodiation/desodiation capacities are 281 and 233 mAh/g, respectively, leading to a high first-cycle Coulombic efficiency of 83%. This is one of the highest first-cycle Coulombic efficiency values reported for carbon-based anodes in NIBs.[48] We also compare the capacity contributions from the sloping regions in the sodiation and desodiation profiles, 128 and 96 mAh/g, respectively. The irreversible capacity loss from the sloping region is 32 mAh/g for G-HC, lower than 43 mAh/g of HC. It is known that SEI typically forms during the sloping region of the first sodiation. The less capacity loss from the sloping region of G-HC indicates that the effect of a smaller surface area that does help mitigate the SEI formation, thus enhancing the first-cycle Coulombic efficiency.

Also importantly, G-HC exhibits a much more stable cycling performance than that of HC. Over the following cycles at 20 mA/g, the desodiation capacity of G-HC is stabilized at ∼220 mAh/g whereas HC shows a lower desodiation capacity of ∼170 mAh/g (Figure 4c). After cycling at 20 mA/g for 10 cycles, the cycling is conducted with various current densities, ranging from 40 to 1000 mA/g. Evidently, G-HC exhibits a higher capacity than HC at all current densities (Figure 4c). When the current density is switched back to 20 mA/g, G-HC exhibits a desodiation capacity of 235 mAh/g, compared to 151 mAh/g for HC. Then, both G-HC and HC are cycled at 20 mA/g for a long-term cycling. After the total 300 cycles, G-HC still retains a desodiation capacity of 213 mAh/g, compared to 54 mAh/g from HC (Figure 4d).

We are also interested in determining the impact from carbon black additive on the performance of hard carbon electrodes. Carbon black (TIMCAL Super C45), 10 wt %, is added into the G-HC electrodes (mass ratio of G-HC/carbon black/PVDF is 8:1:1). As shown in Figure 5a, the first sodiation and desodiation capacity reaches 373 and 289 mAh/g at a current density of 20 mA/g, respectively, compared to 281 and 233 mAh/g without carbon black. Obviously, higher electronic conductivity in the electrode helps enhance the capacity. However, the first-cycle Coulombic efficiency declines from 83% to 78% with the addition of 10 wt % carbon black, which should be attributed to the greater surface area of carbon black (45 m^2/g) and the resulted additional SEI formation. After the first cycle, the desodiation capacity stabilizes at ∼280 mAh/g when cycled at 20 mA/g (Figure 5b). Most importantly, G-HC still delivers a desodiation capacity of 274 mAh/g after 195 cycles. It corresponds to capacity retention of 94.8% and the capacity decay is as small as 0.026% per cycle. A few unstable sodiation/desodiation cycles in the cycling curves are due to the temperature change in our laboratories (Figures 4d and 5b).

CONCLUSION

In summary, we have developed a GO-doping strategy for the synthesis of hard carbon with a very low specific surface area. We discovered that GO effectively prevents foaming of sucrose during caramelization or dehydration and also helps spread the burnoff over a wider range of temperatures during pyrolysis. Both factors facilitate the extremely small specific surface area of the final hard carbon product. When evaluated as an anode for NIBs, with a high active mass loading of 2.5 mg/cm^2, we report one of the highest first-cycle Coulombic efficiency of 83% for NIB carbon anodes, compared to 74% from HC. Over 300 cycles, almost no capacity fading is observed for G-HC whereas the conventional HC fades to only 30% of original capacity. When 10 wt % carbon black is added in the G-HC electrode, the desodiation capacity is increased to 280 mAh/g, and quite stable cycling is still achieved.

ASSOCIATED CONTENT

Supporting Information

Digital pictures for a pure sucrose aqueous solution before and after dried at 110 °C and N_2 adsorption/desorption isotherm of HC-S. This material is available free of charge via the Internet at http://pubs.acs.org.

AUTHOR INFORMATION

Corresponding Author

*X. Ji. E-mail: david.ji@oregonstate.edu.

Notes

The authors declare no competing financial interest.

ACKNOWLEDGMENTS

The authors acknowledge the financial support from Advanced Research Projects Agency-Energy (ARPA-E), Department of Energy of the United States, Award number: DE-

DOI: 10.1021/am507679x
ACS Appl. Mater. Interfaces 2015, 7, 2626−2631

AR0000297TDD. We are thankful to Dr. May Nyman and Dr. Sara Goberna-Ferrón for the TGA measurement.

REFERENCES

(1) Simon, P.; Gogotsi, Y.; Dunn, B. Where Do Batteries End and Supercapacitors Begin? *Science* **2014**, *343*, 1210−1211.

(2) Mai, L.; Yang, F.; Zhao, Y.; Xu, X.; Xu, L.; Hu, B.; Luo, Y.; Liu, H. Molybdenum Oxide Nanowires: Synthesis & Properties. *Mater. Today* **2011**, *14*, 346−353.

(3) Yuan, L.; Wang, Z.; Zhang, W.; Hu, X.; Chen, J.; Huang, Y.; Goodenough, J. B. Development and Challenges of $LiFePO_4$ Cathode Material for Lithium-Ion Batteries. *Energy Environ. Sci.* **2011**, *4*, 269−284.

(4) Yaksic, A.; Tilton, J. E. Using the Cumulative Availability Curve to Assess the Threat of Mineral Depletion: The Case of Lithium. *Resour. Policy* **2009**, *34*, 185−194.

(5) Ellis, B. L.; Nazar, L. F. Sodium and Sodium-Ion Energy Storage Batteries. *Curr. Opin. Solid State Mater. Sci.* **2012**, *16*, 168−177.

(6) Slater, M. D.; Kim, D.; Lee, E.; Johnson, C. S. Sodium-Ion Batteries. *Adv. Funct. Mater.* **2013**, *23*, 947−958.

(7) Palomares, V.; Serras, P.; Villaluenga, I.; Hueso, K. B.; Carretero-Gonzalez, J.; Rojo, T. Na-Ion Batteries, Recent Advances and Present Challenges to Become Low Cost Energy Storage Systems. *Energy Environ. Sci.* **2012**, *5*, 5884−5901.

(8) Pan, H.; Hu, Y.-S.; Chen, L. Room-Temperature Stationary Sodium-Ion Batteries for Large-Scale Electric Energy Storage. *Energy Environ. Sci.* **2013**, *6*, 2338−2360.

(9) Hong, S. Y.; Kim, Y.; Park, Y.; Choi, A.; Choi, N.-S.; Lee, K. T. Charge Carriers in Rechargeable Batteries: Na Ions vs. Li Ions. *Energy Environ. Sci.* **2013**, *6*, 2067−2081.

(10) Kim, Y.; Ha, K.-H.; Oh, S. M.; Lee, K. T. High-Capacity Anode Materials for Sodium-Ion Batteries. *Chem.—Eur. J.* **2014**, *20*, 11980−11992.

(11) Cao, Y.; Xiao, L.; Wang, W.; Choi, D.; Nie, Z.; Yu, J.; Saraf, L. V.; Yang, Z.; Liu, J. Reversible Sodium Ion Insertion in Single Crystalline Manganese Oxide Nanowires with Long Cycle Life. *Adv. Mater.* **2011**, *23*, 3155−3160.

(12) Yabuuchi, N.; Kajiyama, M.; Iwatate, J.; Nishikawa, H.; Hitomi, S.; Okuyama, R.; Usui, R.; Yamada, Y.; Komaba, S. P2-Type Nax $[Fe_{1/2}Mn_{1/2}]$ O_2 Made From Earth-Abundant Elements for Rechargeable Na Batteries. *Nat. Mater.* **2012**, *11*, 512−517.

(13) Liu, Y.; Xu, Y.; Han, X.; Pellegrinelli, C.; Zhu, Y.; Zhu, H.; Wan, J.; Chung, A. C.; Vaaland, O.; Wang, C.; Hu, L. Porous Amorphous $FePO_4$ Nanoparticles Connected by Single-Wall Carbon Nanotubes for Sodium Ion Battery Cathodes. *Nano Lett.* **2012**, *12*, 5664−5668.

(14) Li, S.; Dong, Y.; Xu, L.; Xu, X.; He, L.; Mai, L. Effect of Carbon Matrix Dimensions on the Electrochemical Properties of $Na_3V_2(PO_4)_3$ Nanograins for High-Performance Symmetric Sodium-Ion Batteries. *Adv. Mater.* **2014**, *26*, 3545−3553.

(15) Zhu, H.; Lee, K. T.; Hitz, G. T.; Han, X.; Li, Y.; Wan, J.; Lacey, S.; Cresce, A. v. W.; Xu, K.; Wachsman, E.; Hu, L. Free-Standing $Na_{2/3}Fe_{1/2}Mn_{1/2}O_2$@Graphene Film for a Sodium-Ion Battery Cathode. *ACS Appl. Mater. Interfaces* **2014**, *6*, 4242−4247.

(16) Asher, R. C. A Lamellar Compound of Sodium and Graphite. *J. Inorg. Nucl. Chem.* **1959**, *10*, 238−249.

(17) Ge, P.; Fouletier, M. Electrochemical Intercalation of Sodium in Graphite. *Solid State Ionics* **1988**, *30*, 1172−1175.

(18) Nobuhara, K.; Nakayama, H.; Nose, M.; Nakanishi, S.; Iba, H. First-Principles Study of Alkali Metal-Graphite Intercalation Compounds. *J. Power Sources* **2013**, *243*, 585−587.

(19) Jache, B.; Adelhelm, P. Use of Graphite as a Highly Reversible Electrode with Superior Cycle Life for Sodium-Ion Batteries by Making Use of Co-intercalation Phenomena. *Angew. Chem., Int. Ed.* **2014**, *53*, 10169−10173.

(20) Qian, J.; Chen, Y.; Wu, L.; Cao, Y.; Ai, X.; Yang, H. High Capacity Na-Storage and Superior Cyclability of Nanocomposite Sb/C Anode for Na-Ion Batteries. *Chem. Commun.* **2012**, *48*, 7070−7072.

(21) Zhu, Y.; Han, X.; Xu, Y.; Liu, Y.; Zheng, S.; Xu, K.; Hu, L.; Wang, C. Electrospun Sb/C Fibers for a Stable and Fast Sodium-Ion Battery Anode. *ACS Nano* **2013**, *7*, 6378−6386.

(22) Liu, Y.; Xu, Y.; Zhu, Y.; Culver, J. N.; Lundgren, C. A.; Xu, K.; Wang, C. Tin-Coated Viral Nanoforests as Sodium-Ion Battery Anodes. *ACS Nano* **2013**, *7*, 3627−3634.

(23) Farbod, B.; Cui, K.; Kalisvaart, W. P.; Kupsta, M.; Zahiri, B.; Kohandehghan, A.; Lotfabad, E. M.; Li, Z.; Luber, E. J.; Mitlin, D. Anodes for Sodium Ion Batteries Based on Tin−Germanium−Antimony Alloys. *ACS Nano* **2014**, *8*, 4415−4429.

(24) Zhu, H.; Jia, Z.; Chen, Y.; Weadock, N.; Wan, J.; Vaaland, O.; Han, X.; Li, T.; Hu, L. Tin Anode for Sodium-Ion Batteries Using Natural Wood Fiber as a Mechanical Buffer and Electrolyte Reservoir. *Nano Lett.* **2013**, *13*, 3093−3100.

(25) Xiong, H.; Slater, M. D.; Balasubramanian, M.; Johnson, C. S.; Rajh, T. Amorphous TiO_2 Nanotube Anode for Rechargeable Sodium Ion Batteries. *J. Phys. Chem. Lett.* **2011**, *2*, 2560−2565.

(26) Jian, Z.; Zhao, B.; Liu, P.; Li, F.; Zheng, M.; Chen, M.; Shi, Y.; Zhou, H. Fe_2O_3 Nanocrystals Anchored onto Graphene Nanosheets as the Anode Material for Low-Cost Sodium-Ion Batteries. *Chem. Commun.* **2014**, *50*, 1215−1217.

(27) Su, D.; Ahn, H.-J.; Wang, G. SnO_2@Graphene Nanocomposites as Anode Materials for Na-Ion Batteries with Superior Electrochemical Performance. *Chem. Commun.* **2013**, *49*, 3131−3133.

(28) Yu, D. Y. W.; Prikhodchenko, P. V.; Mason, C. W.; Batabyal, S. K.; Gun, J.; Sladkevich, S.; Medvedev, A. G.; Lev, O. High-Capacity Antimony Sulphide Nanoparticle-Decorated Graphene Composite as Anode for Sodium-Ion Batteries. *Nat. Commun.* **2013**, *4*, DOI:10.1038/ncomms3922.

(29) David, L.; Bhandavat, R.; Singh, G. MoS_2/Graphene Composite Paper for Sodium-Ion Battery Electrodes. *ACS Nano* **2014**, *8*, 1759−1770.

(30) Qu, B.; Ma, C.; Ji, G.; Xu, C.; Xu, J.; Meng, Y. S.; Wang, T.; Lee, J. Y. Layered SnS_2-Reduced Graphene Oxide Composite - A High-Capacity, High-Rate, and Long-Cycle Life Sodium-Ion Battery Anode Material. *Adv. Mater.* **2014**, *26*, 3854−3859.

(31) Dahn, J. R.; Sleigh, A. K.; Shi, H.; Reimers, J. N.; Zhong, Q.; Way, B. M. Dependence of the Electrochemical Intercalation of Lithium in Carbons on The Crystal Structure of the Carbon. *Electrochim. Acta* **1993**, *38*, 1179−1191.

(32) Dahn, J. R.; Zheng, T.; Liu, Y.; Xue, J. S. Mechanisms for Lithium Insertion in Carbonaceous Materials. *Science* **1995**, *270*, 590−593.

(33) Doeff, M. M.; Ma, Y.; Visco, S. J.; De Jonghe, L. C. Electrochemical Insertion of Sodium into Carbon. *J. Electrochem. Soc.* **1993**, *140*, L169−L170.

(34) Stevens, D. A.; Dahn, J. R. High Capacity Anode Materials for Rechargeable Sodium-Ion Batteries. *J. Electrochem. Soc.* **2000**, *147*, 1271−1273.

(35) Stevens, D. A.; Dahn, J. R. The Mechanisms of Lithium and Sodium Insertion in Carbon Materials. *J. Electrochem. Soc.* **2001**, *148*, A803−A811.

(36) Thomas, P.; Billaud, D. Electrochemical Insertion of Sodium into Hard Carbons. *Electrochim. Acta* **2002**, *47*, 3303−3307.

(37) Wenzel, S.; Hara, T.; Janek, J.; Adelhelm, P. Room-Temperature Sodium-Ion Batteries: Improving the Rate Capability of Carbon Anode Materials by Templating Strategies. *Energy Environ. Sci.* **2011**, *4*, 3342−3345.

(38) Tang, K.; Fu, L.; White, R. J.; Yu, L.; Titirici, M.-M.; Antonietti, M.; Maier, J. Hollow Carbon Nanospheres with Superior Rate Capability for Sodium-based Batteries. *Adv. Energy Mater.* **2012**, *2*, 873−877.

(39) Wang, H.; Wu, Z.; Meng, F.; Ma, D.; Huang, X.; Wang, L.; Zhang, X. Nitrogen-Doped Porous Carbon Nanosheets as Low-Cost, High-Performance Anode Material for Sodium-Ion Batteries. *ChemSusChem* **2013**, *6*, 56−60.

(40) Winter, M.; Novak, P.; Monnier, A. Graphites for Lithium-Ion Cells: The Correlation of the First-Cycle Charge Loss with the

DOI: 10.1021/am507679x
ACS Appl. Mater. Interfaces 2015, 7, 2626−2631

Brunauer-Emmett-Teller Surface Area. *J. Electrochem. Soc.* **1998**, *145*, 428−436.
(41) Bommier, C.; Luo, W.; Gao, W.-Y.; Greaney, A.; Ma, S.; Ji, X. Predicting Capacity of Hard Carbon Anodes in Sodium-Ion Batteries Using Porosity Measurements. *Carbon* **2014**, *76*, 165−174.
(42) Hong, K.; Qie, L.; Zeng, R.; Yi, Z.; Zhang, W.; Wang, D.; Yin, W.; Wu, C.; Fan, Q.; Zhang, W.; Huang, Y. Biomass Derived Hard Carbon Used as a High Performance Anode Material for Sodium Ion Batteries. *J. Mater. Chem. A* **2014**, *2*, 12733−12738.
(43) Peled, E. The Electrochemical Behavior of Alkali and Alkaline Earth Metals in Nonaqueous Battery Systems—The Solid Electrolyte Interphase Model. *J. Electrochem. Soc.* **1979**, *126*, 2047−2051.
(44) Ein-Eli, Y. A New Perspective on the Formation and Structure of the Solid Electrolyte Interface at the Graphite Anode of Li-Ion Cells. *Electrochem. Solid-State Lett.* **1999**, *2*, 212−214.
(45) Fong, R.; von Sacken, U.; Dahn, J. R. Studies of Lithium Intercalation into Carbons Using Nonaqueous Electrochemical Cells. *J. Electrochem. Soc.* **1990**, *137*, 2009−2013.
(46) Chevallier, F.; Gautier, S.; Salvetat, J. P.; Clinard, C.; Frackowiak, E.; Rouzaud, J. N.; Béguin, F. Effects of Post-Treatments on the Performance of Hard Carbons in Lithium Cells. *J. Power Sources* **2001**, *98*, 143−145.
(47) Cao, Y.; Xiao, L.; Ai, X.; Yang, H. Surface-Modified Graphite as an Improved Intercalating Anode for Lithium-Ion Batteries. *Electrochem. Solid-State Lett.* **2003**, *6*, A30−A33.
(48) Li, Y.; Xu, S.; Wu, X.; Yu, J.; Wang, Y.; Hu, Y.-S.; Li, H.; Chen, L.; Huang, X. Amorphous Monodispersed Hard Carbon Micro-Spherules Derived from Biomass as a High Performance Negative Electrode Material for Sodium-Ion Batteries. *J. Mater. Chem. A* **2015**, *3*, 71−77.
(49) Buiel, E.; Dahn, J. R. Li-Insertion in Hard Carbon Anode Materials for Li-Ion Batteries. *Electrochim. Acta* **1999**, *45*, 121−130.
(50) Al-Muhtaseb, S. A.; Ritter, J. A. Preparation and Properties of Resorcinol−Formaldehyde Organic and Carbon Gels. *Adv. Mater.* **2003**, *15*, 101−114.
(51) Lin, C.; Ritter, J. A. Carbonization and Activation of Sol−Gel Derived Carbon Xerogels. *Carbon* **2000**, *38*, 849−861.
(52) Ding, J.; Wang, H.; Li, Z.; Kohandehghan, A.; Cui, K.; Xu, Z.; Zahiri, B.; Tan, X.; Lotfabad, E. M.; Olsen, B. C.; Mitlin, D. Carbon Nanosheet Frameworks Derived from Peat Moss as High Performance Sodium Ion Battery Anodes. *ACS Nano* **2013**, *7*, 11004−11015.
(53) Lotfabad, E. M.; Ding, J.; Cui, K.; Kohandehghan, A.; Kalisvaart, W. P.; Hazelton, M.; Mitlin, D. High-Density Sodium and Lithium Ion Battery Anodes from Banana Peels. *ACS Nano* **2014**, *8*, 7115−7129.
(54) Hummers, W. S.; Offeman, R. E. Preparation of Graphitic Oxide. *J. Am. Chem. Soc.* **1958**, *80*, 1339−1339.
(55) Luo, W.; Wang, B.; Wang, X.; Stickle, W. F.; Ji, X. Production of Graphene by Reduction Using a Magnesiothermic Reaction. *Chem. Commun.* **2013**, *49*, 10676−10678.
(56) Krishnan, D.; Raidongia, K.; Shao, J.; Huang, J. Graphene Oxide Assisted Hydrothermal Carbonization of Carbon Hydrates. *ACS Nano* **2013**, *8*, 449−457.
(57) Sun, Y.; Hu, X.; Luo, W.; Huang, Y. Self-Assembled Hierarchical MoO_2/Graphene Nanoarchitectures and Their Application as a High-Performance Anode Material for Lithium-Ion Batteries. *ACS Nano* **2011**, *5*, 7100−7107.
(58) Zhu, Y.; Murali, S.; Cai, W.; Li, X.; Suk, J. W.; Potts, J. R.; Ruoff, R. S. Graphene and Graphene Oxide: Synthesis, Properties, and Applications. *Adv. Mater.* **2010**, *22*, 3906−3924.

DOI: 10.1021/am507679x
ACS Appl. Mater. Interfaces 2015, 7, 2626−2631